Propagation and material-interface effects in the higher-order harmonic radiation from solid-state samples

M. Kolesik

James Wyant College of Optical Sciences, University of Arizona, Tucson, Arizona 85721, USA

The propagation effects reshaping the excitation pulse are known to exhibit a strong influence on the high-harmonic generation (HHG) in solid-state media. Previous measurements showed that the midinfrared pulse dynamics, most importantly the nonlinear loss and spectral broadening, can dampen or even extinguish the highest harmonic peaks. Despite the importance of these effects, their inclusion in the HHG modeling has been so far restricted to one-dimensional propagation and/or very thin samples. This work demonstrates an approach where the driving pulse is simulated with a full spatial and temporal resolution in samples of realistic thickness while the material interfaces are included as well. We show that the HHG spectrum measured in the transmission geometry is greatly affected by the Fresnel reflections causing interference in the vicinity of the material surface, and we find that different parts of the harmonic spectra originate from different regions of the material sample. Our results underline the importance of realistic and comprehensive simulations in the interpretation of high-harmonic generation from solids in the transmission geometry.

I. INTRODUCTION

Higher-order harmonic generation (HHG) from solids [1–3] is an extreme nonlinear effect caused by nonresonant optical excitation at high field-intensities. While it is very much a universal behavior found in many systems exposed to a strong excitation away from resonance, the underlying dynamics also reflects the properties of the given material. This is why the observations of the above-the-gap harmonic generation from a solid-state medium [4] motivated research to understand HHG as an experimental probe. For example, a proof of principle was demonstrated early [5] for the all-optical reconstruction of the electronic band structure using the measured HHG spectra, and similar-in-spirit investigations continue [6,7] to attract interest. Beyond the energy bands, HHG was identified as a suitable probing mechanism also for the light-coupling transition-dipole moments [8,9], and as a way to study the topological properties of materials [10,11] and special features of the material's electronic structure [12,13].

The fact that HHG is so sensitive to every aspect of the microscopic dynamics suggests that the HHG-based spectroscopy may offer many different modalities. However, precisely because the HHG measurements respond to so many properties at the same time, it is not trivial to disentangle the observations. For example, if a thicker sample produces a much weaker harmonic band, is the reason to be attributed solely to the energy loss of the driving pulse, is it rather due to absorption of the harmonic radiation in the material, or perhaps both mechanisms are important? This is the reason why numerical modeling becomes crucial.

However, numerical simulations involving HHG [14,15] are still rather challenging. One of the issues is that a measured HHG spectrum is a manifestation of an interplay between the microscopic nonlinear response and macroscopic propagation [14] of the midinfrared and high-harmonic fields. The numerical complexity of a comprehensive simulation is probably the main reason the modeling of solid-state HHG often concentrates on what can be dubbed a "point response," which is calculated at a single location in the material under the assumption that the local electric field is known. The spectrum of the current density simulated at a single point is then taken to represent the measured HHG spectrum. Obviously, this is a rather poor approximation, especially in the transmission geometry.

When the solid-state high-harmonic spectra are generated in the transmission geometry, the measured spectrum is greatly affected by the dynamics of the driving pulse. The most important mechanism, identified, e.g., in [16] in experiments on GaAs, is the high intensity of the driver pulse causing carrier generation. The associated losses can significantly decrease the energy of the pulse by the time it reaches the exit facet of the sample, from where most of the high-harmonic radiation is generated. As a result, the higher harmonic orders are effectively "extinguished." The self-phase modulation is also significant and it causes spectral broadening of all high-harmonic peaks. For these reasons, the reflection geometry offers a more direct probe of the microscopic material dynamics [17–19]. Nevertheless, it is important to understand the requirements for an accurate interpretation of the transmission-geometry high-harmonic spectra (THHG). Comprehensive modeling, which includes the simulation of the excitation pulse, can be instrumental in this.

Extending the numerical simulation of HHG beyond the "point-model" level presents a formidable challenge. While it is understood that the geometry of the experiment [16] together with the propagation effects [20–22] play a role
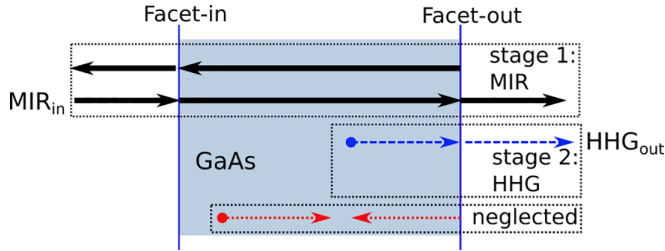
FIG. 1. Simulation strategy: The electromagnetic field is split into computational components. Thick solid black arrows represent the incident pulse, the forward and backward MIR radiation inside the sample, and also the eventually reflected radiation. Thin dashed blue arrows show the high-harmonic radiation which is generated in the vicinity of the output facet, together with the corresponding radiation transmitted to the outside of the sample (which is what we aim to calculate). Dotted thin red arrows indicate the high-harmonic radiation generated deep inside the sample and also the radiation internally reflected from the output facet; both are neglected in our simulation (see text).

in shaping the measured HHG, comprehensive simulations based on first principles, being numerically very expensive [20,23,24], are usually reduced to one-dimensional pulse propagation [25] and/or are only applied to very thin material slabs. However, under highly nonlinear conditions and/or in a realistically thick sample (hundreds of microns), the propagation dynamics couples temporal and spatial degrees of freedom of the excitation pulse and the one-dimensional approximation becomes insufficient.

The goal of the present work is two-fold. First, from the computational standpoint, we present a scheme which makes it feasible to create a comprehensive model of an experiment in the transmission geometry. The approach accurately treats the propagation effects in both the midinfrared excitation pulse and in the high-frequency radiation, all the while the Fresnel reflections from the internal material boundaries are also included in the simulation. Such calculations can be done with full spatial resolution, and are therefore capable of capturing spatiotemporal coupling in ultrashort duration pulses, which is always significant in samples with realistic thickness.

Second, we put forward new insights into how the above-the-gap harmonic radiation is formed. More specifically, we show that different parts of the HHG spectrum effectively originate from different depths below the sample surface. While the highest harmonics are generated at or very close to the surface, the signal for the medium-order harmonics is sourced much deeper, up to hundreds of nanometers. It is also shown here that the propagation and absorption effects add significantly to the damping of higher harmonic orders.

II. SIMULATION SETUP

It should be useful to describe the simulation setup in broad strokes before discussing details in the following sections. We will also identify and justify the most important approximations. The calculation, schematically depicted in Fig. 1, consists of two distinct stages. It starts with a midinfrared (MIR) pulse incident on a slab of GaAs. Fresnel reflections from the input and output facets of the sample give rise to

wavepackets propagating forward and backward through the material slab. These electromagnetic fields are all fully included in the simulation during the first stage, and are also mutually coupled through the reflections from the material interfaces. The purpose of the first stage is to calculate the MIR waveform in the vicinity of the output facet because that is where the detected high-harmonic radiation originates.

The second stage of the simulation concentrates on the vicinity of the output facet. Here we utilize the recorded field of the MIR waveform to excite the GaAs and produce high-harmonic radiation which partly exits the material. This is the numerically expensive part of the whole simulation because, at each spatial point in the surface layer, one must solve the semiconductor Bloch equations over the entire Brillouin zone. The result of the second stage is the high-harmonic radiation incident on the exit facet of the sample. It is then straightforward to calculate how much of it is transmitted through the material interface and what spectrum is eventually detected in the far field.

The numerical complexity of the microscopic calculations is the main reason we are forced to neglect some of the high-frequency radiation propagating though the material. Namely, we do not include the high-harmonic radiation that is generated deep in the volume of the material. We also neglect the high frequencies internally reflected from the output facet. The strong material absorption prevents this radiation from contributing to the measured HHG spectra.

However, we also neglect the carriers excited into conduction bands when the high-harmonic radiation is absorbed. It is conceivable that these excitations could affect the HHG process. Indeed, it was suggested in [25] that such a process, called self-seeding, can enhance the harmonic cutoff.

The reason we do not think the inclusion of this effect would influence our conclusions is that once both stages are finished, we can verify that the radiation produced in stage two does not change the resulting HHG spectra when it is added to the MIR driving pulse. We perform this check at several spatial points in the vicinity of the sample surface, and we indeed find that the spectra with and without the high-frequency radiation included in the excitation pulse are extremely similar. Only slight differences are found around the harmonic band closest to the band gap, and the differences at higher frequencies are negligible. This gives us the confidence that the separation of the simulation into two stages is appropriate.

III. EVOLUTION EQUATIONS FOR PULSED ELECTROMAGNETIC FIELDS

The description of the solid-state high-harmonic generation can be often treated in the first Born approximation in the sense that one first calculates the evolution of the optical field for the excitation pulse, including all necessary frequencies below the band gap. The results are then used to drive the high-harmonic generation for the frequency range above the material band gap. While this is an approximation, it is an excellent one due to the fact that the intensity of the high-harmonic radiation is so low, and it is absorbed so quickly, that the feedback effect on the propagation of the driving pulse is truly negligible. Note that such a splitting of the simulation

into a "driver" and "harmonic stage" has been utilized in the high-harmonic generation modeling in gaseous media [26] as well.

A. Excitation-pulse dynamics inside a slab sample

Consider a material sample characterized by its frequency-dependent permittivity $\epsilon(\omega)$, in a plane-parallel slab geometry. The material is exposed to the excitation by an optical pulse incident on the "entrance facet," not necessarily in the normal direction. The Fresnel reflections from the material interfaces give rise to multiple pulses propagating inside the slab in "forward" and "backward" directions. For a very short incident pulse and a sufficiently thick sample these counterpropagating waveforms do not overlap or interact in the bulk of the material. However, the incident and reflected pulses always overlap in the vicinity of the exit surface, where they create an interference pattern. The interference between the pulses can be especially pronounced in materials with higher refractive indices, and the effect this has on the harmonic generation is amplified by the extreme nonlinearity of the conversion process. This situation must be accurately captured by the simulation of the excitation pulse.

1. Propagation inside the bulk material

Away from the material boundaries, the displacement field can be decomposed into forward- and backward-propagating components

$$\vec{D} = \vec{D}_+ + \vec{D}_- , \tag{1}$$

each expressed as a superposition of plane waves inside the slab

$$\vec{D}_\pm(t, \vec{r}) = \int \vec{A}_\pm(t, \vec{k}) e^{\mp i\omega(k)t} e^{i\vec{k}\cdot\vec{r}} d^3k . \tag{2}$$

Here $\omega(k)$ is treated as a function of the spatial frequency and it satisfies the dispersion relation

$$k^2 = \omega(k)^2 \epsilon(\omega(k))/c^2, \quad k = |\vec{k}| . \tag{3}$$

Since this relation defines $\omega(k)$ as an implicit function, the treatment must be restricted to a single transparency window so that a unique complex-valued frequency can be assigned to a given wave number k. Here we apply this framework to the below-gap frequencies to describe the pump pulses, including their spectral broadening and below-gap harmonic generation.

In a complete analogy to the t-propagated unidirectional pulse propagation equation [27], the vector spectral amplitudes that appear in (2) obey their individual propagation equations

$$\partial_t \vec{A}_\pm(t, \vec{k}) = \mp \frac{i\omega(k)}{2} e^{\pm i\omega(k)t} \left[\frac{k^2 - \vec{k}\vec{k}}{k^2} \cdot \vec{P}(\vec{k}) - \mu_0 \partial_t \vec{J}(\vec{k}) \right]. \tag{4}$$

However, these evolution equations must be solved simultaneously because they are coupled via the light-matter interaction in the slab, here expressed as the induced polarization $\vec{P}$ and current density $\vec{J}$

$$\vec{P}(\vec{r}, t) = \vec{P}(\{\vec{E}(\vec{r}, t)\}) \text{ and } \vec{J}(\vec{r}, t) = \vec{J}(\{\vec{E}(\vec{r}, t)\}) . \tag{5}$$

Of course, the polarization calculation requires to obtain the *total* electric field E from the *total* displacement field D, and this can be done by iterative inversion of the constitutive material relation

$$\vec{E} = \frac{1}{\epsilon}[\vec{D} - \vec{P}(\{\vec{E}\})] , \tag{6}$$

as it is usual in the time-domain Maxwell-equations solvers. In a typical high-intensity femtosecond pulse propagation in condensed media, two or three iterations are sufficient. Given a model to calculate the polarization and the current density for a given history of the electric field, the above equations constitute an approximation-free evolution system for the Maxwell problem inside the sample.

2. Treatment of material interfaces

In addition to the nonlinear coupling between the two $D_\pm$, the material material interfaces must be accounted for. Roughly speaking, the idea is to extend the spatial domain in (2) to the outside of the slab so that a spectral propagator can be applied across the whole sample, and also in the regions "behind" the material interfaces. Each of the two $D_\pm$ amplitudes is held by its dedicated computational domain in which the *linear* propagation is strictly unidirectional [and governed by $\epsilon(\omega)$]. These domains extend beyond the boundary of the material slab by some 50 to 100 microns (along the beam direction, say z) to accommodate their "input" and "output" ports."

The artificial output-region extending the computational domain outside the exit facet allows the spectral propagator to evolve the optical wave-packet encountering the material interface beyond the material boundary. However, the optical field amplitude outside of the sample is never used except to calculate the spatial spectrum of the pulse via Fourier transform. The extended domain is eventually terminated by an apodized absorbing region serving as a pulse dump.

On the entrance-side of the computational domain, the field outside the entrance facet must be constructed anew before each application of the linear propagator as if the waveform propagated from a half-space space filled by the same medium. However, the precalculated field in the input port must correctly account for the reflection from the material boundary. This is achieved by a mapping of the field propagating in the slab in the opposite direction, while applying the wave-number-dependent Fresnel reflection coefficient, $r(k_z, k_\perp)$, in the spectral representation of the pulse.

To illustrate the algorithm in a pseudocode, consider how the right-going field $D^+(z, r_\perp)$ partially reflects from the exit facet located at $z = z_0$ and is used to prepare the input port for the left-going field $D^-(z, r_\perp)$ for locations $z > z_0$, i.e., behind the material interface. A single update is executed as follows:

(1) right-going $D^+(z, r_\perp)$ obtained in the previous step;
(2) calculate spatial spectrum $D^+(z, r_\perp) \to \hat{D}^+(k_z, k_\perp)$;
(3) apply reflection coefficient $r(k_z, k_\perp)\hat{D}^+(k_z, k_\perp)$;
(4) back to real space, $D_r^+(z, r_\perp) \leftarrow r(k_z, k_\perp)\hat{D}^+(k_z, k_\perp)$;
(5) recalculate $D^-(z_0 + z, r_\perp) = D_r^+(z_0 - z, r_\perp)$ for $z > z_0$.

Here, $\to$ and $\leftarrow$ stand for the transforms between the real-space and spectral-space representations, each consisting of

a Fourier transform connecting z, k_z and a Hankel transform connecting $r_\perp, k_\perp$.

This treatment of the internal reflections provides a numerically exact solution to the linear part of the propagation problem, with the accuracy controlled by the extension of the spatial domain along the pulse propagation direction. Of course, the spatial extension together with two additional spectral transform make this algorithm expensive in comparison with unidirectional propagation. However, this is a nonissue given that the calculations required to model the material microscopic response (see Sec. III B) are orders of magnitude more expensive.

B. Propagation of harmonic radiation

Having calculated $\vec{E}(\vec{r}, t)$ inside the sample, we can use it in point-by-point microscopic calculations to evaluate the induced current density $\vec{J}(\vec{r}, t)$ which is responsible for the above-the-gap harmonic radiation. This is done using the methods described in the subsequent sections (Sec. III B). Here we give a description of how the source $\vec{J}(\vec{r}, t)$ converts into HHG radiation detected outside of the sample.

In general, the HHG radiation detected outside of the sample is sourced in a subsurface layer several microns thick. Thus, the first step is to propagate the HHG radiation generated in the depth of the sample to its surface. In the second step, each spectral component is transmitted through the material interface with a frequency-dependent Fresnel coefficient. Because of the highly nonlinear dependence of the induced current density on the local amplitude of the driving field, the transverse profile of the beam plays a role and it is crucial to account for it.

The propagation of the high-harmonic radiation through the sample is governed by the unidirectional pulse propagation equation [28] for the spectral amplitude $\vec{S}(z, \omega, k_\perp)$ of the electric field

$$\partial_z \vec{S}(z, \omega, k_\perp) = ik_z \vec{S}(z, \omega, k_\perp) - \frac{\omega}{2\epsilon_o c^2 k_z} \vec{J}(z, \omega, k_\perp), \quad (7)$$

where the propagation constant $k_z \equiv \sqrt{\omega^2/c^2 \epsilon(\omega) - k_\perp^2}$ reflects the absorption and dispersion properties for the above-the-gap frequencies via $\epsilon(\omega)$, and $\vec{J}(z, \omega, k_\perp)$ is the spatial spectrum of the current density induced by the driver field. In the first Born approximation, the above is nothing but a set of inhomogeneous first-order differential equations that are straightforward to solve.

Because the beam spot is usually at least several μm in size, it is admissible to use a paraxial approximation for the short-wavelength HHG radiation. This amounts to replacing the propagation constant by $k_z(\omega) = \omega n(\omega)/c$ in (7). Further, the spectrum is measured in the far field, and therefore the detected amplitude we are interested in is $\vec{S}(z, \omega, k_\perp = 0)$. The solution for the detected spectral amplitude of HHG then reads

$$\vec{S}(z, \omega, 0) \sim \frac{\omega t(\omega)}{2\epsilon_o c^2 k_z(\omega)} \int^z e^{ik_z(\omega)(z-z')} \vec{J}(z', \omega, 0) dz', \quad (8)$$

where $t(\omega)$ stands for the Fresnel transmission coefficient (at normal incidence), and where the on-axis far field amplitude of the induced current density can be calculated as the integral
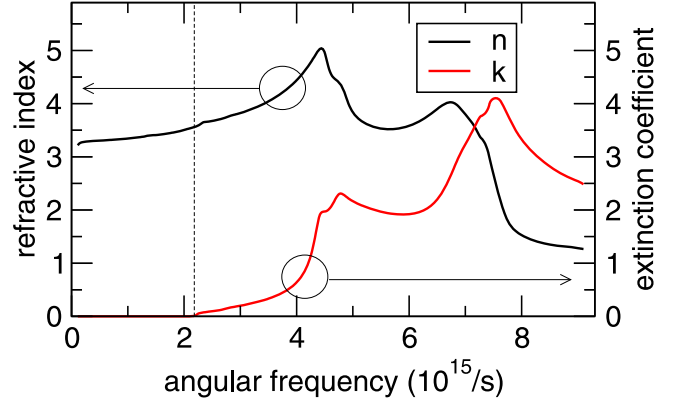

FIG. 2. Refractive index and extinction coefficient in GaAs.

over the beam cross section

$$\vec{J}(z', \omega, 0) \sim \int \vec{J}(z', \omega, r) r \, dr . \quad (9)$$

This formula represents the coherent average over the excitation beam, and has a significant effect on the resulting spectrum.

The most pronounced effect embodied in the above formulas is the frequency-dependent absorption manifested in propagator $e^{ik_z(\omega)(z-z')}$. It will be shown in the following that it is the interplay between the HHG absorption and the spatially modulated source strength in $J(z', \omega, r)$ that controls which regions in the sample contribute most to the detected HHG spectrum.

IV. MATERIAL MODELS

This work utilizes a model of zinc blende materials for our simulation-based illustration. In particular, we concentrate on GaAs because it is the material for which the propagation effects in HHG were studied in some detail [16].

A. Linear optical properties

The GaAs model for the linear chromatic properties was constructed by joining three different sets of data, obtained from [29] and originally published in [30–32]. Figure 2 illustrates the refractive index and extinction coefficient utilized for the simulation of the propagation of the high-harmonic radiation.

These data are used to construct the frequency-dependent propagation constant $k_z(\omega)$ in the paraxial-propagation formula (7). The tabulated $n(\omega)$ is also used to calculate the frequency-dependent "coupling prefactor" in front of the convolution integral.

B. Nonlinear material response

The nonlinear response of the material is calculated in the framework of semiconductor Bloch equations (SBE) [33], which in turn requires a description of the electronic structure. For the band structure we utilize the semi-empirical tight-binding model [34] with specific parameter sets representing GaAs adopted from [35]. These material models are utilized and tested in the previous works, demonstrating that
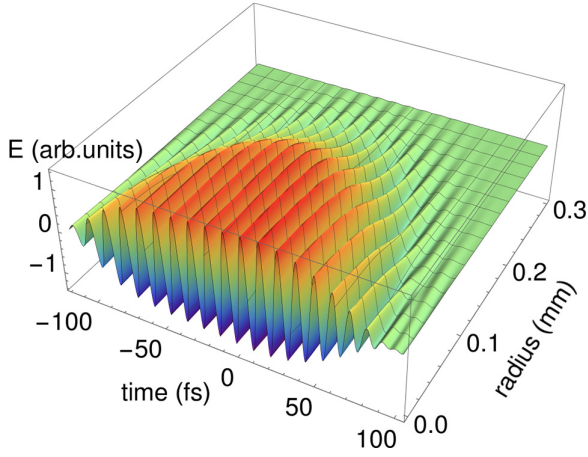
FIG. 3. Spatiotemporal map of the electric field in the driving pulse, depicted after 650 μm propagation through a GaAs sample. The color scheme was chosen to emphasize the flat-top shape in what was initially a Gaussian pulsed beam.

the second-order nonlinear coefficient in GaAs [36] can be calculated, and that measurements of HHG spectra were also reproduced without resorting to any parameter tuning [37]. The sgiSBEs simulator, described in [38], calculates the time-dependent density matrix $\rho_{mn}(\mathbf{k};t)$ for each initial $\mathbf{k}$, and gives the induced current-density as an integral over the Brillouin zone [39]

$$\mathbf{j}(t) = \sum_{mn} \int_{\mathrm{BZ}} \mathrm{Tr}[\partial_{\mathbf{k}_t} h(\mathbf{k}_t) \rho(\mathbf{k};t)] \frac{d\mathbf{k}}{(2\pi)^3} \,, \qquad (10)$$

where the $\mathbf{k}$-dependent Hamiltonian $h(\mathbf{k})$ and its gradient is obtained in an explicit form from the tight-binding model and $\mathbf{k}_t = \mathbf{k} - \mathbf{A}(t)$ is slaved to the vector potential of the driving pulse.

The initial density matrix is set to represent all valence bands full and the conduction bands empty. Each evolution step follows a scheme akin to the operator splitting, alternating between the density matrix ρ_{o} in the atomic-orbital basis, or ρ_{h} in the instantaneous Hamiltonian basis as follows:

(1) $\rho_{\mathrm{o}}(\mathbf{k}, t - \Delta t)$ obtained in the previous step;

(2) diagonalization of $h(\mathbf{k}_t)$ yields:

(I) eigenvectors organized into matrix V,

(II) energies ϵ_a forming matrix $U = \mathrm{diag}\{-i\Delta t \epsilon_a/\hbar\}$;

(3) transformation to Hamiltonian basis, $\rho_{\mathrm{h}} \leftarrow V \rho_{\mathrm{o}} V^\dagger$;

(4) evolution step, $\rho_{\mathrm{h}} \leftarrow U \rho_{\mathrm{h}} U^\dagger$;

(5) off-diagonal dephasing, $\rho_{\mathrm{h}} \leftarrow \rho_{\mathrm{h}} \exp[-\Delta t/\tau_{\mathrm{dep}}]$;

(6) transformation to orbital basis, $\rho_{\mathrm{o}} \leftarrow V^\dagger \rho_{\mathrm{h}} V$;

(7) microscopic current, $j(\mathbf{k}, t) \leftarrow \mathrm{Tr}[\partial_{\mathbf{k}_t} h(\mathbf{k}_t) \rho_{\mathrm{o}}(\mathbf{k};t)]$.

While this implementation of the algorithm [38] minimizes the number of matrix-matrix multiplication, the overall numerical complexity is mainly given by the exact diagonalization step, and that is why ours is a relatively expensive algorithm. The advantage of this approach is that the symmetry of the material is faithfully preserved and that the noise floor of the method is very low.

The phenomenological dephasing time τ_{dep} is chosen to be 5 fs. It was observed in [37] (cf. Fig. 3) that the convergence of a simulated spectrum as a function of the number of

Brillouin-zone grid points is faster for shorter τ_{dep}. This is why, for this relatively fast dephasing, we can sample the Brillouin zone with a rather low resolution of 16^3 grid points and already obtain decent simulated spectra. While an accurate convergence would require grids about three times as big as those used here, all we need for the present purpose is a model with a qualitatively correct behavior. In other words, with finer grid-resolutions the calculations would be much more expensive, but our conclusions would not change. In fact, it is safe to say that the same conclusions can be reached with any HHG model that can capture the symmetry of the material.

V. RESULTS

We assume that a Gaussian pulse, with a central wavelength of 3.5 μm, has a peak intensity of 10^9 V/m in the material just after entering the sample. The transverse size of the collimated beam is chosen to be 0.3 mm, so that the diffraction effects remain weak during its propagation through material layers from tens to hundreds of microns. The cross section of the beam is sampled on a radial grid of 32 points (spaced suitably for the discrete Hankel transform [40]). The excitation pulse is polarized linearly along the crystal axis, resulting in a geometry with a vanishing second-order nonlinearity. The nonlinear light-matter interaction included in the driver simulation are the instantaneous Kerr effect (with $n_2 = 1.2 \times 10^{-17}$ m²/W [41,42]), and the generation of excited carriers. The latter is described by a phenomenological rate [43] scaling with I^3 and prefactor adjusted such that the "ionization" losses through a sample 650 μm thick are about 50 percent for the given initial peak amplitude, roughly matching the losses observed in the experiment of [16], which motivated our simulation setup. The methods outlined in Sec. II A are utilized for the first stage of the simulation involving the excitation pulse. We use spatial grids of up to 2^{18} points (along z) with a grid-spacing of 5 nm and record the history of the electric field inside a 2 μm layer adjacent to the exit facet of the sample. The recording at each spatial point used 8192 sampling points over a time-interval of 600 fs.

In the second stage of the simulation, we utilize the scheme described in Sec. II B to simulate the generated high-harmonic radiation and its propagation from the sample towards its detection in the far field. The electric-field histories recorded in the first stage are used as the excitation for the simulation of the material response relevant for the above-the-gap frequency region as described in Sec. III.

A. Propagation effects and space-time reshaping of the excitation pulse

Let us first illustrate the spatial-and-temporal reshaping the excitation pulse goes through. Already after 50 microns of propagation, the pulse energy and amplitude of an originally Gaussian pulse diminish significantly, and the waveform continues to reshape upon further propagation. Current carriers are mainly generated in the high-intensity on-axis region, and cause a nonlinear phase shift which adds curvature to the wave fronts in the trailing portion of the pulse. The amplitude reshaping is illustrated in Fig. 3, showing the driving pulse
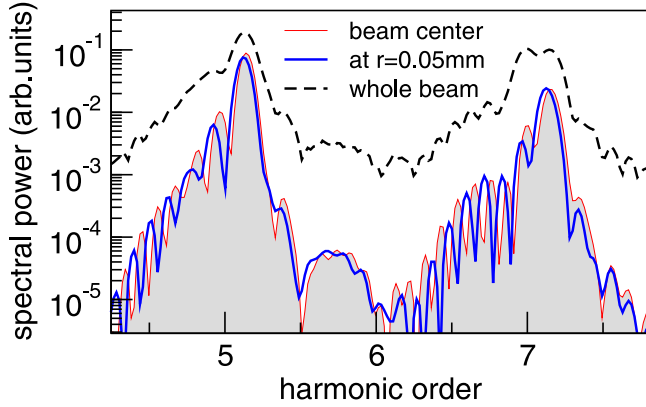
FIG. 4. Spectral power of the induced current density exhibits modulations caused by the chirp of the driver pulse. The "phase shift" between the modulations at different radial locations reflects different timing of the harmonic radiation at different radii.

resolved in radius and local time. Note that this "snapshot" is taken before the pulse reaches the exit facet of the sample. The color scheme in the figure is chosen to emphasize the most important feature, which is the flat-top peak amplitude. This is a consequence of the losses induced by the carrier excitation, which affect most the highest-intensity parts of the waveform, and which effectively "shaved-off" the top of the original Gaussian pulse.

The phase shifts in the carrier wave modify the timing of the induced nonlinear current density. In particular, the chirp gives a temporal shift between harmonics radiated by the leading and trailing parts of the driver pulse. This shows up in the harmonic spectra as a modulation, exemplified in Fig. 4, where we show a detail of the spectral power of the induced current density in the center of the beam compared to its counterpart at the radial distance of 50 micron. While the two spectra exhibit the same power levels, their modulation structures are shifted in relation to each other. This indicates that different phase shift in the carrier at different radial distance cause different relative timing between spectral components of the nonlinear current. These are the effects that a simple intensity averaging [20] would not capture properly, and this is why we calculate the microscopic response of the material from the actual radially resolved time-dependent electric fields.

B. Interference effects at the exit facet

Related to the propagation effects is the Fresnel reflection of the driving pulse from the material interfaces. The internal reflection from the exit facet may be especially important because it can significantly alter the peak amplitude of the driving pulse.

In the particular setting of this work, the reflections from the material interfaces play a major role. The reason is illustrated in Fig. 5, showing the inside of the material slab 10 μm thick, irradiated by a pulse entering from the left. Depicted here is the cycle-averaged local intensity of the "composite" optical waveform which consists of pulses propagating forth and back as in a Fabry-Perot cavity. The most important feature is the interference pattern in the vicinity of the exit facet,
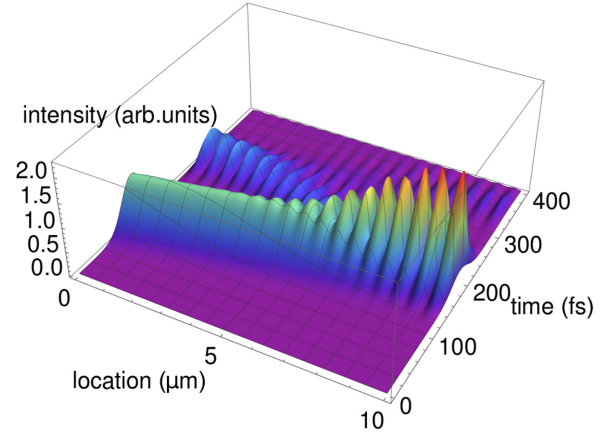

FIG. 5. Cycle-averaged light intensity versus time and location in the sample of GaAs. Entrance and exit facets are located at the left-side edge of the figure (i.e., at $z = 0\,\mu m$), and right at the location of right-most peak, respectively. Materials with high refractive indices, such as GaAs, give rise to a pronounced interference structure near the exit facet which in turn affects the nonlinear material response.

where the local intensity reaches considerably higher than in the incident pulse. Here, the intensity profile is extended and drawn one quarter wavelength beyond the exit facet of the sample in order to indicate the depth of the modulation, which is significant due to the high refractive index of the material.

Given the extreme nonlinearity of the high-harmonic generation process, the peak amplitude modulations in the vicinity of the exit sample-facet have significant effect on the HHG spectrum, as we show next. While simulating the driver-pulse propagation in the GaAs sample, we record the time-dependent electric field within a layer adjacent to the exit facet. Throughout this layer, the microscopic response of the material is calculated as described in Sec. III B, giving the induced current density $\vec{J}(r, z, t)$, Fourier transform of which enters as the source in the propagation equations (7) for the high-harmonic radiation.

The logarithmic-scale spectral power of this source, $S = \log_{10}(|J(r = 0, z, \omega)|^2)$, is shown in Fig. 6. It is evident that
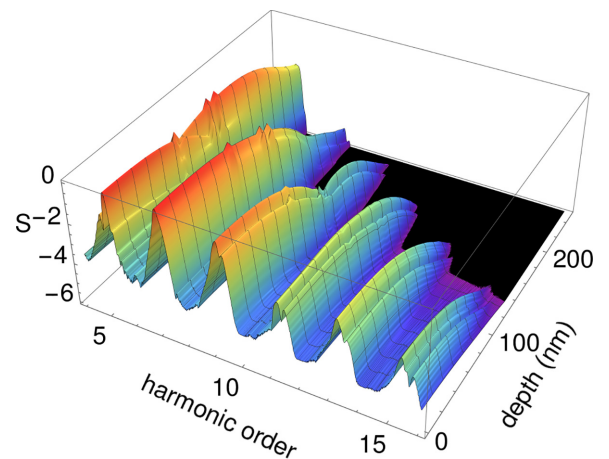

FIG. 6. Logarithmic spectral power of the induced current density, $S = \log_{10}(|J(r = 0, z, \omega)|^2)$, as a function of the depth beneath the exit facet of the sample. This example is for GaAs slab 170 μm thick, excited by a 60 fs pulse centered at $\lambda = 3.5\,\mu m$.
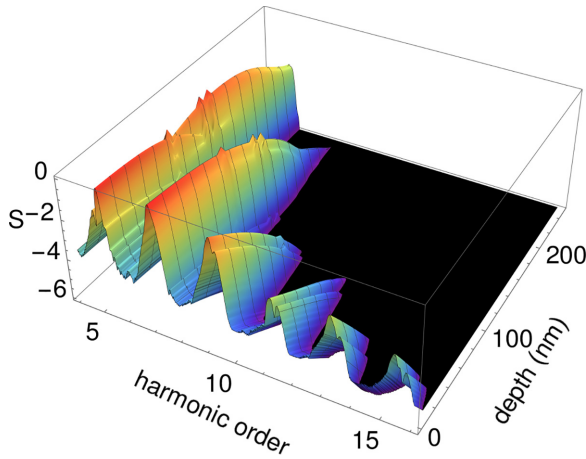
FIG. 7. Spectral power of the high-harmonic generation detected at the exit facet, shown here as a function of the depth in the sample where the radiation was emitted. Contributions from the deeper regions are effectively extinguished in the highest harmonic bands.

as the local amplitude of the excitation field diminishes deeper from the sample surface, the induced current exhibits orders of magnitude weaker high-frequency bands. This is a manifestation of the interference fringe in the driving pulse localized at the sample facet. Of course, even deeper into the sample, where the MIR intensity increases again in the second fringe, HHG spectra power also increases. However, due to the absorption of the above-the-gap frequencies, those deeper regions give negligible contributions to the observed HHG spectrum.

C. Propagation and absorption of the high-harmonic radiation

In HHG simulations, the spectral power of the induced current is often assumed to approximate the actual observed HHG spectrum, essentially neglecting the difference between a source term in the Maxwell equations and the radiation the term generates. In this section we show that it is an utterly unrealistic assumption for the transmission geometry where the propagation effects shape the spectral content of the high-harmonic radiation.

The relevant relation between the source term $J(\omega)$ and the spectrum of the detected radiation, $S(\omega)$, is expressed in (8) which accounts for the propagation and absorption of HHG radiation from its source to outside of the sample. To appreciate the absorption and its effect on the reshaping of the HHG spectrum, Fig. 7 depicts the spectral power sourced at a given depth as it arrives at the sample surface. More precisely, the quantity shown is $S = \log_{10}(|e^{ik_z(\omega)z}J(z, \omega, 0)|^2)$, so that the effect of the absorption can be appreciated.

The contrast with Fig. 6 is indeed stark, especially for higher-harmonic orders. Only a very thin surface layer contributes to the highest observed orders, and this is obviously due to the fact that a few hundred nanometers of the material suffices to attenuate the radiation that was generated deeper in the sample. In contrast, the lower above-the-gap harmonics carry contributions from a much thicker layer of the material.
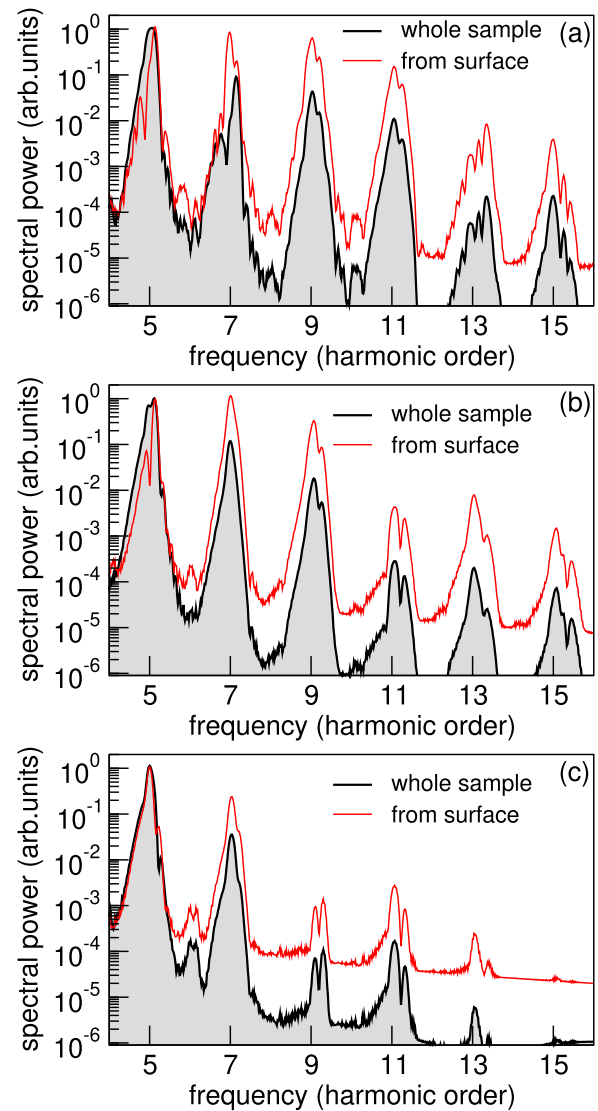

FIG. 8. The effect of the propagation and absorption in the above-gap harmonic radiation for (a) 45, (b) 170, and (c) 650 μm thick material sample. HHG spectra obtained solely from the surface overestimate the higher harmonic bands. This "damping effect" is in addition to that due to the nonlinear absorption of the pump.

D. HHG spectra observed outside the material sample

While the previous illustration shows the frequency-dependent attenuation effect of the material between the origin of the radiation and the surface, it says little about the actually detected spectrum. To calculate this, formula (8) calls for a "coherent sum" of all contributions from the depths of the sample.

Figure 8 shows the results for three different sample thicknesses, namely 45, 170, and 650 microns. The spectra measured in the far field outside the sample are shown as the gray-shaded area below the thick black line. In a qualitative agreement with the experimental observations in [16], it is evident that the thicker samples effectively suppress the higher harmonic orders. While the main reason for this was identified as due to the propagation effects reshaping and attenuating the MIR driver pulse, here we show that that the

propagation effects experienced by the high-harmonic radiation itself are equally important. To make this point, each panel also depicts a HHG spectrum (top, red line) calculated from the naive assumption that the observed signal is dominated by its strongest component originating right at the sample surface. In other words, such a calculation accounts for the propagation effects of the driver pulse, but neglects the propagation effects acting on the high-harmonic radiation. As one can see, neglecting the latter gives spectra that overestimate the spectral power of the higher-harmonic bands by more than an order of magnitude.

VI. CONCLUSION

We presented a framework integrating realistic HHG simulations into a comprehensive model of an experiment in the transmission geometry, where the propagation effects experienced by the excitation pulse influence the measurements in a crucial way. Our approach represents a numerically less demanding alternative to the time-domain denstiy functional theory (DFT) simulations of the material coupled with the one-dimensional wave equation for the electromagnetic field. An important advantage of the method we put forward is the ability to simulate realistically thick samples while including a full-resolution three-dimensional (3D) description of the pulsed beam which is necessary to capture its spatial and temporal reshaping.

Our results were in line with some previously discussed propagation effects. In particular, we corroborated the role of the nonlinear absorption [16,22,25] and self-phase modulation of the excitation pulse [16,22]. We also verified the importance of the spectral averaging caused by the intensity variation in the cross section of the beam [20,44]. Beyond the previously discussed propagation effects, we identified several additional mechanisms that were equally important or perhaps even more consequential in shaping the HHG spectra measured in the transmission geometry.

The first effect is the *spatial-temporal* reshaping of the excitation pulse which influences how different parts of the cross section in the pulsed beam contribute to the measured spectrum. As the excitation waveform propagates through the material, it excites current carriers which in turn impart time- and radially dependent nonlinear phase-shifts. As a consequence, the high harmonics generated at different radii emerge with different timings and varying chirps, giving rise to "point spectra" with pronounced modulations structures. The measured far-field spectrum, being a coherent sum over the cross section of the beam, appears much smoother.

Second, we showed that the interference effects created by the Fresnel reflections at the output facet of the sample substantially change the peak amplitude, and this has a pronounced effect on the resulting HHG spectrum. Due to the extreme nonlinear nature of the HHG process, neglecting the role of the material interface underestimates the relevant peak amplitudes and gives much weaker high-harmonic spectra.

Third, and the most important, is the propagation effect in the HHG radiation itself. As the HHG radiation propagates through the material before it exits from the sample, the absorption adds significantly to the damping of the higher-order harmonic bands. These propagation effects together with the spatial modulation of the nonlinear material response decide which region of the sample contributes most to a given portion of the spectrum. While the highest orders are generated only in a very thin surface layer, medium-order harmonics are sourced from the deeper regions of of the material. An important implication here is that a "point-model response" simulated at a single spatial location does not provide a good approximation of the actual HHG spectrum.

Our results also imply that the propagation-induced effective dephasing put forward in [21] is unlikely to affect the transmission HHG spectra because the mechanism in [21] requires propagation distances longer than the very short path traveled by the high-harmonic radiation which eventually reaches the detector.

The main takeaway from our study is that no quantitative or even semi-quantitative interpretation of the HHG spectrum taken in the transmission geometry is possible without a comprehensive modeling which includes the $(3D + 1)$ simulation of the excitation pulse, sample geometry including Fresnel reflections from its facets, and the propagation of the HHG radiation through the lossy material. However, our work also demonstrates that, thanks to the natural separation between the dynamics of the below- and above-the-gap frequencies, it is possible to construct realistic HHG models at an acceptable computational cost. While many of the HHG experiments with solid-state materials are done in the transmission geometry, accurate simulations should facilitate their interpretation.

[1] E. Goulielmakis and T. Brabec, Nat. Photon. **16**, 411 (2022).

[2] S. Ghimire and D. A. Reis, Nat. Phys. **15**, 10 (2019).

[3] J. Park, A. Subramani, S. Kim, and M. F. Ciappina, Adv. Phys.: X **7**, 2003244 (2022).

[4] S. Ghimire, A. D. DiChiara, E. Sistrunk, P. Agostini, L. F. DiMauro, and D. A. Reis, Nat. Phys. **7**, 138 (2011).

[5] G. Vampa, T. J. Hammond, N. Thiré, B. E. Schmidt, F. Légaré, C. R. McDonald, T. Brabec, D. D. Klug, and P. B. Corkum, Phys. Rev. Lett. **115**, 193603 (2015).

[6] A. A. Lanin, E. A. Stepanov, A. B. Fedotov, and A. M. Zheltikov, Optica **4**, 516 (2017).

[7] A. J. Uzan-Narovlansky, A. Jiménez-Galán, G. Orenstein, R. E. F. Silva, T. Arusi-Parpar, S. Shames, B. D. Bruner, B. Yan, O. Smirnova, M. Ivanov, and N. Dudovich, Nat. Photon. **16**, 428 (2022).

[8] Y. Qiao, Y.-Q. Huo, S.-C. Jiang, Y.-J. Yang, and J.-G. Chen, Opt. Express **30**, 9971 (2022).

[9] Y. Qiao, Y. Huo, H. Liang, J. Chen, W. Liu, Y. Yang, and S. Jiang, Phys. Rev. B **107**, 075201 (2023).

[10] D. Baykusheva, A. Chacón, J. Lu, T. P. Bailey, J. A. Sobota, H. Soifer, P. S. Kirchmann, C. Rotundu, C. Uher, T. F. Heinz, D. A. Reis, and S. Ghimire, Nano Lett. **21**, 8970 (2021).

[11] G. Bae, Y. Kim, and J. D. Lee, Phys. Rev. B **106**, 205422 (2022).

[12] A. J. Uzan, G. Orenstein, A. Jiménez-Galán, C. McDonald, R. E. F. Silva, B. D. Bruner, N. D. Klimkin, V. Blanchet, T. Arusi-Parpar, M. Krüger, A. N. Rubtsov, O. Smirnova, M. Ivanov, B. Yan, T. Brabec, and N. Dudovich, Nat. Photon. **14**, 183 (2020).

[13] C. P. Schmid, L. Weigl, P. Grössing, V. Junk, C. Gorini, S. Schlauderer, S. Ito, M. Meierhofer, N. Hofmann, D. Afanasiev, J. Crewse, K. A. Kokh, O. E. Tereshchenko, J. Güdde, F. Evers, J. Wilhelm, K. Richter, U. Höfer, and R. Huber, Nature (London) **593**, 385 (2021).

[14] L. Yue and M. B. Gaarde, J. Opt. Soc. Am. B **39**, 535 (2022).

[15] C. Yu, S. Jiang, and R. Lu, Adv. Phys.: X **4**, 1562982 (2019).

[16] P. Xia, C. Kim, F. Lu, T. Kanai, H. Akiyama, J. Itatani, and N. Ishii, Opt. Express **26**, 29393 (2018).

[17] F. Sekiguchi, M. Sakamoto, K. Nakagawa, H. Tahara, S. A. Sato, H. Hirori, and Y. Kanemitsu, Phys. Rev. B **108**, 205201 (2023).

[18] P. Peterka, A. Slobodeniuk, T. Novotný, P. Suthar, M. Bartoš, F. Trojánek, P. Malý, and M. Kozák, APL Photon. **8**, 086103 (2023).

[19] P. Suthar, F. Trojánek, P. Malý, T.-Y. Derrien, and M. Kozák, Commun. Phys. **7**, 104 (2024).

[20] I. Floss, C. Lemell, G. Wachter, V. Smejkal, S. A. Sato, X.-M. Tong, K. Yabana, and J. Burgdörfer, Phys. Rev. A **97**, 011401(R) (2018).

[21] I. Kilen, M. Kolesik, J. Hader, J. V. Moloney, U. Huttner, M. K. Hagen, and S. W. Koch, Phys. Rev. Lett. **125**, 083901 (2020).

[22] M. Hussain, S. Kaassamani, T. Auguste, W. Boutu, D. Gauthier, M. Kholodtsova, J.-T. Gomes, L. Lavoute, D. Gaponov, N. Ducros, S. Fevrier, R. Nicolas, T. Imran, P. Zeitoun, G. O. Williams, M. Fajardo, and H. Merdji, Appl. Phys. Lett. **119**, 071101 (2021).

[23] S. Yamada, T. Otobe, D. Freeman, A. Kheifets, and K. Yabana, Phys. Rev. B **107**, 035132 (2023).

[24] M. Uemoto and K. Yabana, Opt. Express **30**, 23664 (2022).

[25] Y. Lang, Z. Peng, J. Liu, Z. Zhao, and S. Ghimire, Phys. Rev. Lett. **129**, 167402 (2022).

[26] M. B. Gaarde, J. L. Tate, and K. J. Schafer, J. Phys. B: At. Mol. Opt. Phys. **41**, 132001 (2008).

[27] M. Kolesik, J. V. Moloney, and M. Mlejnek, Phys. Rev. Lett. **89**, 283902 (2002).

[28] M. Kolesik and J. V. Moloney, Phys. Rev. E **70**, 036604 (2004).

[29] M. N. Polyanskiy, Sci. Data **11**, 94 (2024).

[30] D. E. Aspnes, S. M. Kelso, R. A. Logan, and R. Bhat, J. Appl. Phys. **60**, 754 (1986).

[31] T. Skauli, P. S. Kuo, K. L. Vodopyanov, T. J. Pinguet, O. Levi, L. A. Eyres, J. S. Harris, M. M. Fejer, B. Gerard, L. Becouarn, and E. Lallier, J. Appl. Phys. **94**, 6447 (2003).

[32] K. Papatryfonos, T. Angelova, A. Brimont, B. Reid, S. Guldin, P. R. Smith, M. Tang, K. Li, A. J. Seeds, H. Liu, and D. R. Selviah, AIP Adv. **11**, 025327 (2021).

[33] M. Lindberg and S. W. Koch, Phys. Rev. B **38**, 3342 (1988).

[34] A. D. Carlo, Semicond. Sci. Technol. **18**, R1 (2002).

[35] P. Vogl, H. P. Hjalmarson, and J. D. Dow, J. Phys. Chem. Solids **44**, 365 (1983).

[36] M. Kolesik, Opt. Lett. **48**, 3191 (2023).

[37] M. Kolesik and J. V. Moloney, Phys. Rev. B **108**, 115433 (2023).

[38] J. Gu and M. Kolesik, Phys. Rev. A **106**, 063516 (2022).

[39] J. Wilhelm, P. Grössing, A. Seith, J. Crewse, M. Nitsch, L. Weigl, C. Schmid, and F. Evers, Phys. Rev. B **103**, 125419 (2021).

[40] H. F. Johnson, Comput. Phys. Commun. **43**, 181 (1987).

[41] W. C. Hurlbut, Y.-S. Lee, K. L. Vodopyanov, P. S. Kuo, and M. M. Fejer, Opt. Lett. **32**, 668 (2007).

[42] T. R. Ensley and N. K. Bambha, Opt. Express **27**, 37940 (2019).

[43] A. Couairon, E. Brambilla, T. Corti, D. Majus, O. d. J. Ramírez-Góngora, and M. Kolesik, Eur. Phys. J. Spec. Top. **199**, 5 (2011).

[44] C. Q. Abadie, M. Wu, and M. B. Gaarde, Opt. Lett. **43**, 5339 (2018).